Supporting Information for

Nanoserpents: Graphene Nanoribbon Motion on Two-Dimensional Hexagonal Materials

Wengen Ouyang, Davide Mandelli, Michael Urbakh, Oded Hod*

School of Chemistry, and The Sackler Center for Computational Molecular and Materials Science, Tel Aviv University, Tel Aviv 6997801, Israel.

Corresponding Author

* E-mail: urbakh@post.tau.ac.il

* Phone: +9726408324

This supporting information document includes the following sections:

1. Refined Fitting Parameters of the Registry Dependent Interlayer Potential for Graphene and *h*-BN

The registry dependent interlayer potential (ILP) and the Kolmogorov Crespi (KC) potential have the following general pairwise form:[1-3]

$$V(\mathbf{r}_{ij}, \mathbf{n}_i, \mathbf{n}_j) = \mathrm{Tap}(r_{ij})\left[V_{\mathrm{att}}(r_{ij}) + V_{\mathrm{Rep}}(\mathbf{r}_{ij}, \mathbf{n}_i, \mathbf{n}_j) + V_{\mathrm{Coul}}(r_{ij})\right]. \quad \text{(S1)}$$

Here, $V_{\mathrm{att}}(r_{ij})$, $V_{\mathrm{Rep}}(\mathbf{r}_{ij}, \mathbf{n}_i, \mathbf{n}_j)$, and $V_{\mathrm{Coul}}(r_{ij})$ correspond to the long-range van der Waals attraction, short-range Pauli repulsion, and monopolar electrostatic interactions, respectively. These terms take different forms in the KC and ILP potentials as detailed below. $\mathbf{r}_{ij}$ is the vector distance between atoms i and j residing on different layers, while $\mathbf{n}_k$ is a unit vector normal to the surface at the k^{th} atomic position. The latter is defined as the average of the three vectors normal to the planes defined by the triangles formed by the k^{th} atom with its three nearest neighbors within the hexagonal lattice. These three normals are calculated as the cross products between the displacement vectors from atomic position k to two of its nearest neighbors, considering each distinct couple of nearest neighbors.[4] In open boundary systems, the atoms at the edges have only one or two nearest neighbors. The normal to an atom having two nearest neighbors is calculated as the cross product between the displacement vectors to its two nearest neighbors. In the case of an atom that has only one nearest neighbor, first the cutoff is adjusted in order to include one or two second nearest neighbors; the normal is then computed following the appropriate procedure out of the two outlined above. The taper function

$$\mathrm{Tap}(r_{ij}) = 20\left(\frac{r_{ij}}{R_{\mathrm{cut},ij}}\right)^7 - 70\left(\frac{r_{ij}}{R_{\mathrm{cut},ij}}\right)^6 + 84\left(\frac{r_{ij}}{R_{\mathrm{cut},ij}}\right)^5 - 35\left(\frac{r_{ij}}{R_{\mathrm{cut},ij}}\right)^4 + 1 \quad \text{(S2)}$$

provides a continuous long-range cutoff (up to third derivative) that dampens the various interactions at interatomic separations larger than $R_{\mathrm{cut},ij}$.

1.1 The Interlayer Potential (ILP)

The analytical form of the long-range attractive term is adapted from the Tkatchenko-Scheffler augmentation scheme[5] to density functional theory (DFT) given by the standard r^{-6} expression dampened at short range by a Fermi-Dirac type function, which in DFT calculations avoids double counting of interactions:

$$V_{\mathrm{att}}(r_{ij}) = -\frac{1}{1+e^{-d_{ij}\left[r_{ij}/\left(s_{R,ij}\cdot r_{ij}^{\mathrm{eff}}\right)-1\right]}}\frac{C_{6,ij}}{r_{ij}^6}. \quad \text{(S3)}$$

Here, $C_{6,ij}$ is the pairwise dispersion coefficient of atoms i and j residing on adjacent layers, r_{ij}^{eff} is the sum of their effective equilibrium vdW atomic radii, and d_{ij} and $s_{R,ij}$ are unit-less parameters defining the steepness and onset of the short-range Fermi−Dirac type damping function.

The repulsive term is written as a combination of isotropic and anisotropic contributions as follows:

$$V_{\text{Rep}}(\mathbf{r}_{ij}, \mathbf{n}_i, \mathbf{n}_j) = e^{\alpha_{ij}\left(1-\frac{r_{ij}}{\beta_{ij}}\right)}\left\{\varepsilon_{ij} + C_{ij}\left[e^{-(\rho_{ij}/\gamma_{ij})^2} + e^{-(\rho_{ji}/\gamma_{ij})^2}\right]\right\}, \tag{S4}$$

where ε_{ij} and C_{ij} are constants that set the energy scales associated with the isotropic and anisotropic repulsion, respectively, β_{ij} and γ_{ij} set the corresponding interaction ranges, and α_{ij} is a parameter that sets the steepness of the isotropic repulsion function. The lateral interatomic distance ρ_{ij} is defined as the shortest distance from atom j to the surface normal, $\mathbf{n}_i$, at the position of atom i:

$$\begin{cases}\rho_{ij}^2 = r_{ij}^2 - (\mathbf{r}_{ij}\cdot\mathbf{n}_i)^2 \\ \rho_{ji}^2 = r_{ji}^2 - (\mathbf{r}_{ji}\cdot\mathbf{n}_j)^2\end{cases}. \tag{S5}$$

The electrostatic term, which appears only in the homogeneous *h*-BN ILP, is given by a shielded monopolar Coulomb expression of the form:

$$V_{\text{Coul}}(r_{ij}) = kq_iq_j/\sqrt[3]{r_{ij}^3 + \lambda_{ij}^{-3}}. \tag{S6}$$

Here, $k = 14.399645\ \text{eV}\cdot\text{Å}\cdot\text{C}^{-2}$ is Coulomb's constant, while q_i and q_j are the effective charges of atoms i and j (residing in different layers) given in units of the absolute value of the electron charge, e, and $\lambda_{ij} = \sqrt{\lambda_{ii}\lambda_{jj}}$ is a shielding parameter used to eliminate the short-range singularity of the electrostatic interaction in regions where the Pauli repulsions between overlapping electron clouds dominate the interlayer potential. In the present study, we used the fixed effective atomic charge approximation adopting values of $q_B = 0.42e$ and $q_N = -0.42e$.[1]

1.2 The Kolmogorov Crespi Potential

The van de Waals attraction term of the KC potential has the following form:[4]

$$V_{\text{att}}(r_{ij}) = -A_{ij}\left(\frac{z_{0,ij}}{r_{ij}}\right)^6, \tag{S7}$$

where A_{ij} and $z_{0,ij}$ are energy and length scale parameters, respectively. The anisotropic repulsion term reads:

$$V_{\mathrm{Rep}}(\mathbf{r}_{ij},\mathbf{n}_i,\mathbf{n}_j)=e^{-\lambda_{ij}(r_{ij}-z_{0,ij})}\left\{C_{ij}+e^{-(\rho_{ij}/\delta_{ij})^2}\left[C_{0,ij}+C_{2,ij}\left(\frac{\rho_{ij}}{\delta_{ij}}\right)^2+C_{4,ij}\left(\frac{\rho_{ij}}{\delta_{ij}}\right)^4\right]+\right.$$
$$\left.e^{-(\rho_{ji}/\delta_{ij})^2}\left[C_{0,ij}+C_{2,ij}\left(\frac{\rho_{ji}}{\delta_{ij}}\right)^2+C_{4,ij}\left(\frac{\rho_{ji}}{\delta_{ij}}\right)^4\right]\right\}, \quad \text{(S8)}$$

where C_{ij}, λ_{ij} and $C_{0/2/4,ij}$, δ_{ij} are energy and length scale parameters of the isotropic and anisotropic repulsion terms, respectively.

In the original KC potential, no continuous long-range cut-off is applied. If, as often done to reduce computational burden, one applies a step-like long-range cutoff, this assumption leads to a discontinuity at the cut-off radius, which can lead to difficulties in energy minimization and loss of energy conservation in dynamics simulations. To avoid these problems, we have also considered a modified version of the KC potential where the expressions of and in Eq. S7 and Eq. S8 are multiplied by the smooth taper cutoff function defined in Eq. S2.

Below we provide two sets of refined parameters for the original (without taper function) and the modified (including the taper function) KC potential.

1.3 Fitting procedure

In the expressions presented above, the ILP parameters $\alpha_{ij},\beta_{ij},\gamma_{ij},\varepsilon_{ij},C_{ij},d_{ij},s_{R,ij},r_{ij}^{\mathrm{eff}},C_{6,ij},R_{\mathrm{cut},ij},\lambda_{ij}$ and the KC parameters $z_{0,ij},A_{ij},\delta_{ij},C_{ij},C_{0,ij},C_{2,ij},C_{4,ij},\lambda_{ij}$ serve as fitting parameters. Here, we provide two refined sets of parameters for the registry dependent ILP for homogeneous interfaces of graphene and hexagonal boron nitride (*h*-BN), as well as their heterojunctions and two sets of refined parameters for the KC potential with or without the taper function for graphene based systems. The force-field has been benchmarked against density functional theory calculations of several dimer systems within the Heyd-Scuseria-Ernzerhof hybrid density functional approximation,[6-8] corrected for many-body dispersion effects (see section 2 below).[9, 10] Unlike the previous parametrizations,[1, 2] where the parameters were fitted manually focusing on achieving good agreement only in the long-range interaction regime, in the present parametrization the parameters were fitted using an automatic interior-point technique, as implemented in MATLAB,[11, 12] which improved the agreement with the reference DFT data across the entire interaction region.

Our training set included three periodic structures (graphene/graphene, graphene/*h*-BN and *h*-BN/*h*-BN)

and 10 finite structures (Benzene dimer, Borazine dimer, $B_{12}N_{12}H_{12}$ dimer, Coronene dimer, Benzene/Coronene, Borazine/$B_{12}N_{12}H_{12}$, Benzene/Borazine, Benzene/$B_{12}N_{12}H_{12}$, Borazine/Coronene and Coronene/$B_{12}N_{12}H_{12}$). The reference data consisted of binding energy curves (Figure S1-S3) and sliding energy surfaces (Figure S4-S5) of all systems. The latter were computed fixing the equilibrium interlayer distance to that of the optimal stacking mode of the corresponding periodic structures. For the case of heterogeneous graphene/*h*-BN junctions we considered two binding energy curves calculated at the optimal (C-) and worst (A-) stacking modes.[2]

Table S1: List of ILP parameter values for graphene and *h*-BN based systems. The training set includes all the binding energy curves and all the sliding potential surfaces mentioned in the text. A value of $R_{\mathrm{cut}} = 16$ Å is used throughout.

	β_{ij} (Å)	α_{ij}	γ_{ij} (Å)	ε_{ij} (meV)	C_{ij} (meV)	d_{ij}	$s_{R,ij}$	$r_{eff,ij}$ (Å)	$C_{6,ij}$ (eV•Å^6)	λ_{ij} (Å^{-1})
C-C	3.2058	7.5111	1.2353	1.53E-05	37.5304	15.4999	0.7954	3.6814	25.7145	--
B-B	3.1437	9.8251	1.9364	2.7848	14.4960	15.1993	0.7834	3.6829	49.4980	0.70
N-N	3.4432	7.0845	1.7473	2.9140	46.5086	15.0204	0.8008	3.5518	14.8102	0.69
H-H	3.9745	6.5380	1.0806	0.6701	0.8334	15.0224	0.7491	2.7672	1.6160	--
C-B	3.3037	10.5441	2.9267	16.7200	0.3572	15.3053	0.7002	3.0973	30.1629	--
C-N	3.2536	8.8259	1.0595	18.3447	21.9136	15.0000	0.7235	3.0131	19.0631	--
B-N	3.2953	7.2243	2.8727	1.3715	0.4347	14.5946	0.8044	3.7657	24.6700	0.694982
C-H	2.6429	12.9141	1.0203	0.9750	25.3410	15.2229	0.8116	3.8873	5.6875	--
B-H	2.7187	9.2146	3.2731	14.0157	14.7605	15.0848	0.7768	3.6409	7.9642	--
N-H	2.7535	8.2267	3.1064	0.8074	0.3944	15.0332	0.7451	2.7336	3.8462	--

The fitting procedure involved two steps. First, we fitted the parameters for the three periodic structures, using both the binding energy curves and the sliding potential surfaces. This provided us with the C-C, B-B, N-N, C-B, C-N, and B-N sets of parameters. Next, we fixed these parameters and fitted the remaining

H-H, C-H, B-H, and N-H parameter sets using the reference data corresponding to the finite dimers. In this final stage we introduced a weighting factor proportional to the dimer size to increase the importance of the larger dimers during the fitting procedure. The resulting ILP parameters are presented in Table S1.

Table S2: List of ILP parameter values for graphene and *h*-BN based systems. The training set is the same as that of Table S1 apart for the exclusion of the binding energy curve calculated at the A-stacking mode of the graphene/*h*-BN junction. A value of $R_{\mathrm{cut}} = 16$ Å is used throughout.

	β_{ij} (Å)	α_{ij}	γ_{ij} (Å)	ε_{ij} (meV)	C_{ij} (meV)	d_{ij}	$s_{R,ij}$	$r_{eff,ij}$ (Å)	$C_{6,ij}$ (eV•Å^6)	λ_{ij} (Å^{-1})
C-C	3.2058	7.5111	1.2353	1.53E-05	37.5304	15.4999	0.7954	3.6814	25.7145	--
B-B	3.1437	9.8251	1.9364	2.7848	14.4960	15.1993	0.7834	3.6829	49.4980	0.70
N-N	3.4432	7.0845	1.7473	2.9140	46.5086	15.0204	0.8008	3.5518	14.8102	0.69
H-H	3.4994	6.5011	1.4887	0.0044	2.1538	15.2527	0.7090	2.6454	1.3485	--
C-B	3.0957	11.4129	3.5402	0.0067	0.0021	15.4960	0.7727	3.3415	31.1639	--
C-N	3.2371	8.3963	1.5489	18.2309	31.8545	15.0000	0.8100	3.7858	18.8623	--
B-N	3.2953	7.2243	2.8727	1.3715	0.4347	14.5946	0.8044	3.7657	24.6700	0.694982
C-H	2.6478	10.7335	5.9574	37.2437	0.7124	15.2182	0.7126	2.6665	5.8883	--
B-H	2.6498	9.8478	2.9422	0.3973	22.1276	15.4635	0.8498	3.4991	6.4569	--
N-H	2.8599	8.5956	5.6698	0.0080	0.0039	15.1037	0.8499	3.4995	3.1446	--

The training set for the parameters presented in Table S1 included the binding energy curve of the energetically least favorable A-stacked graphene/*h*-BN junction. As a consequence, for the heterojunction we observe a somewhat larger deviation of the ILP results from the reference sliding energy potential compared to that obtained in the homogeneous cases (see Figure S4 and Figure S5). In Table S2 we present a second set of ILP parameters that was obtained excluding the A-stacked graphene/*h*-BN binding energy curve from the training set, which improves the agreement with the reference DFT data. Specifically, for commensurate heterojunctions we suggest using Table S2 parameters when calculating tribological properties at the equilibrium interlayer distance, whereas Table S1 parameters should be used for

calculations in the sub-equilibrium regime. For incommensurate graphene/*h*-BN heterojunctions the two parameter sets provide similar results at equilibrium interlayer distance (see Figure S7) and can be both used.

The corresponding two sets of refined KC potential parameters without and with the taper function are given in Table S3 and Table S4, respectively.

Table S3: List of KC parameter values for graphene-based systems (original KC, without taper function). The training set includes all the binding energy curves of graphene-based systems and the sliding potential surface of periodic bilayer graphene.

	$z_{0,ij}$ (Å)	$C_{0,ij}$ (meV)	$C_{2,ij}$ (meV)	$C_{4,ij}$ (meV)	C_{ij} (meV)	δ_{ij} (Å)	λ_{ij} (Å^{-1})	A_{ij} (meV)
C-C	3.3288	21.8472	12.0602	4.7111	6.6789E-04	0.77181	3.1439	12.6603
C-H	3.1565	37.4005	8.3911E-03	55.0618	5.18E-05	0.44373	2.5088	11.4791
H-H	2.2188	4.53E-05	4.87E-05	2.02774	1.19395	0.89685	0.238105	9.22E-05

Table S4: List of KC parameter values for graphene-based systems (modified KC, with taper function). The training set includes all the binding energy curves of graphene-based systems and the sliding potential surface of periodic bilayer graphene. A value of $R_{\mathrm{cut}} = 16$ Å is used throughout.

	$z_{0,ij}$ (Å)	$C_{0,ij}$ (meV)	$C_{2,ij}$ (meV)	$C_{4,ij}$ (meV)	C_{ij} (meV)	δ_{ij} (Å)	λ_{ij} (Å^{-1})	A_{ij} (meV)
C-C	3.4161	20.0216	10.90556	4.27566	1.0011E-02	0.84471	2.9361	14.3133
C-H	2.8491	72.5572	1.01642E-02	65.9233	8.79625E-05	0.33492	3.0403	14.7533
H-H	2.1875	3.9158E-05	5.0896E-05	3.6658	1.5374	0.96336	0.42499	1.5707E-04

2. Implementation of the ILP and KC Potentials within the LAMMPS Package and Benchmark Tests

We have implemented the ILP and KC potential within the LAMMPS package for molecular dynamics simulations (Full details regarding the implementation are given in https://lammps.sandia.gov/doc/pair_ilp_graphene_hbn.html and https://lammps.sandia.gov/doc/pair_kolmogorov_crespi_full.html).[13] In the next sections, we report the results of a set of benchmark calculations used to check the agreement between our implementation of the ILP and KC potential and the reference DFT data.

2.1 Binding Energy Curves

Figure S1 presents the binding energy curves calculated for the laterally periodic bilayer structures, using the two sets of parameters reported in Table S1 and Table S2. The refined parameters proposed herein provide a satisfactory agreement with the reference binding energy curve within the long-range, near-equilibrium, and sub-equilibrium interlayer separation regimes. This improves upon our previous parameterizations, which shows large deviations in the sub-equilibrium region.[1, 2] However, we note that the reliability of the reference DFT calculations in the sub-equilibrium region, which is relevant for high pressure and tribological calculations, remains unclear. Hence, our fitting procedure mainly demonstrates the ability to obtain good agreement with reference data across the entire interlayer separation range. Nevertheless, in order to obtain reliable sub-equilibrium ILP results accurate reference data for this region should be provided.

An improved agreement with the reference data is also found for the finite homogenous (Figure S2) and heterogeneous (Figure S3) dimers, with the exception of Borazine. This is due to the weighting technique adopted during the fitting procedure, which gives less importance to the smaller systems (see Section 1).

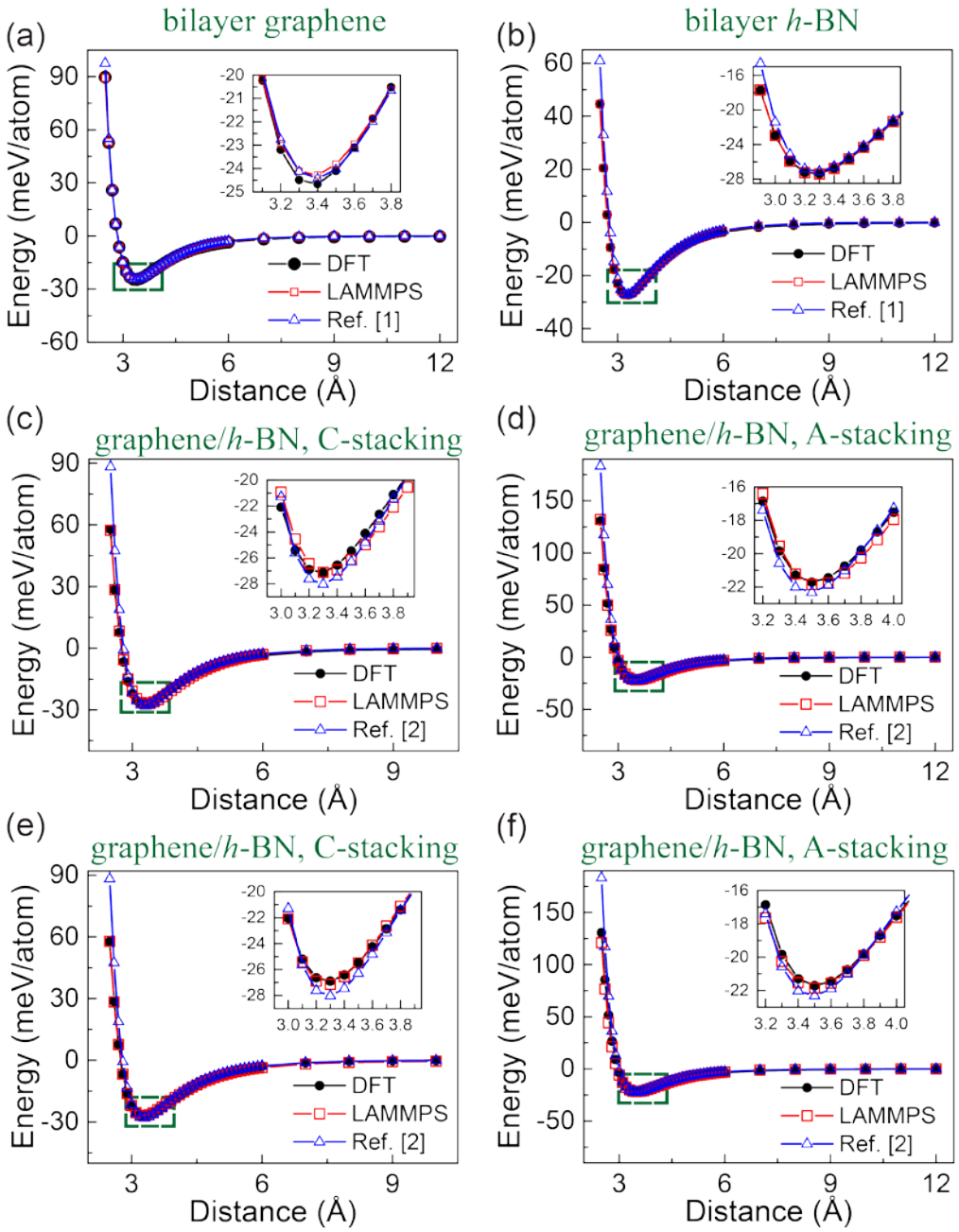

***Figure S1**: Binding energy curves of the laterally periodic bilayer structures of (a) graphene/graphene, (b) h-BN/h-BN, (c),(e) C-stack graphene/h-BN, (d),(f) A-stack graphene/h-BN. The results presented in panels (c) and (d) are calculated with the first set parameters (Table S1) and those presented in panels (e) and (f) are calculated with the second set parameters (Table S2). The reported energies are measured relative to the infinitely separated bilayer value and are normalized by the total number of atoms per unit-cell. The insets provide a zoom-in on the equilibrium interlayer separation region.*

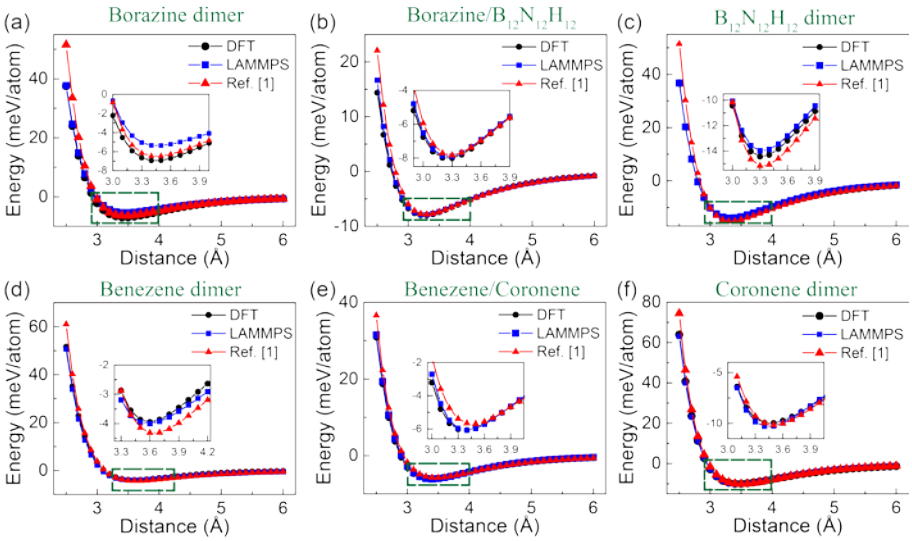

***Figure S2**: Binding energy curves calculated for the finite homogenous dimers of (a) Borazine, (b) Borazine/$B_{12}N_{12}H_{12}$, (c) $B_{12}N_{12}H_{12}$, (d) Benzene, (e) Benzene/Coronene, and (f) Coronene. The reported energies are measured relative to the infinitely separated dimer value and are normalized by the total number of atoms per unit-cell. The insets provide a zoom-in on the equilibrium interlayer separation region. Here, the parameters presented in Table S1 are used. Similar results are obtained when using the parameters of Table S2.*

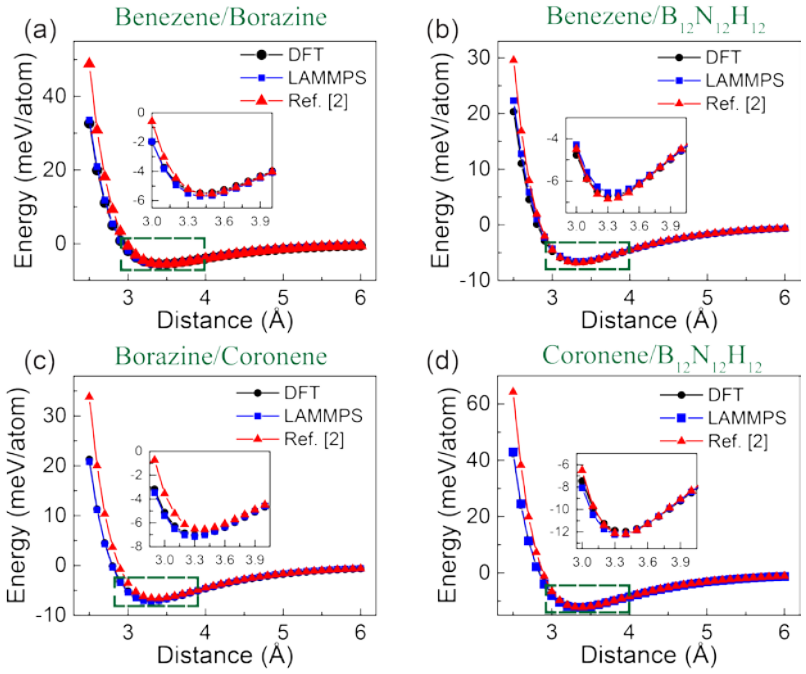

***Figure S3**: Binding energy curves calculated for the finite heterogeneous dimers of (a) Benzene/Borazine, (b) Benzene/ $B_{12}N_{12}H_{12}$, (c) Borazine/Coronene, and (d) Coronene/$B_{12}N_{12}H_{12}$. The reported energies are measured relative to the infinitely separated dimer value and are normalized by the total number of atoms per unit-cell. The insets provide a zoom-in on the equilibrium interlayer separation region. Here, the parameters presented in Table S1 are used. Similar results are obtained when using the parameters of Table S2.*

2.2 Sliding Energy Surfaces

A major advantage of the anisotropic ILP over isotropic pairwise potentials, such as Lennard-Jones and Morse potentials, is its ability to simultaneously capture both the interlayer binding and sliding energy surfaces of layered materials junctions.[1-4]

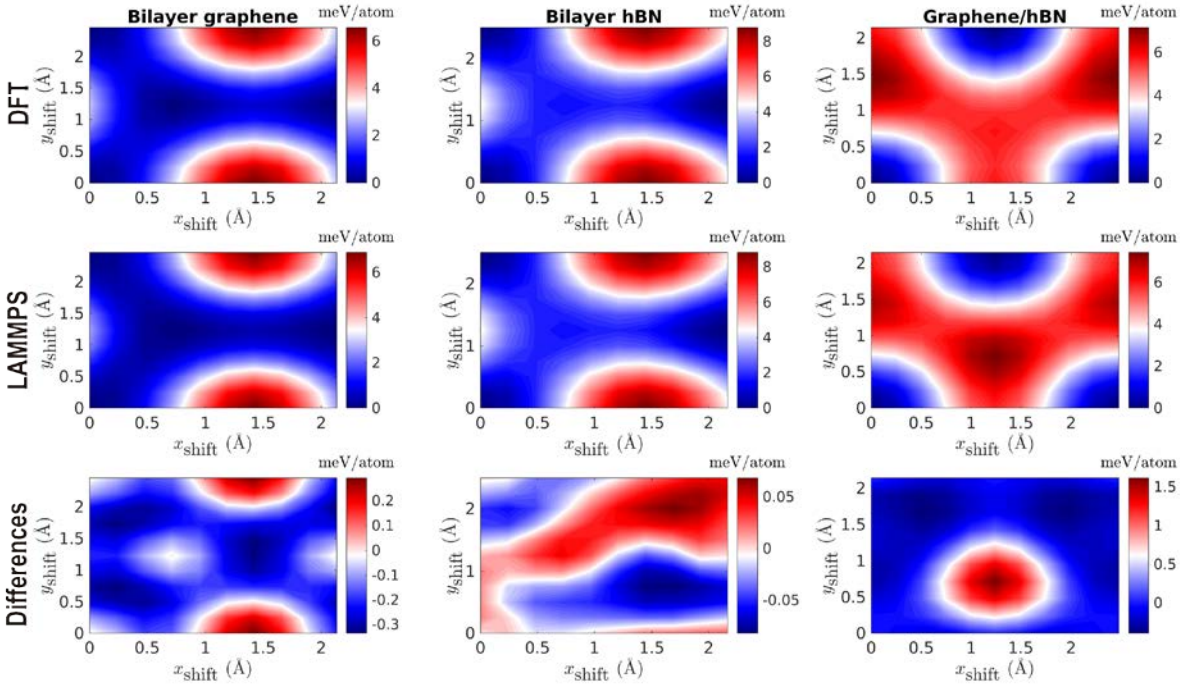

Figure S4*: Sliding energy surfaces of the various periodic structures considered. The first and second rows present the sliding energy surface of graphene/graphene, h-BN/h-BN and graphene/h-BN bilayers calculated using dispersion augmented DFT and the LAMMPS implementation of the refined ILP, respectively. The third row presents their differences. The parameters of Table S1 are used in the ILP calculations.*

This is demonstrated in Figure S4, where the ILP sliding energy surfaces obtained using the parameters of Table S1 for all the periodic structures are compared to the reference DFT data. The first and second rows in Figure S4 present the sliding energy surfaces of graphene/graphene, *h*-BN/*h*-BN and graphene/*h*-BN calculated using DFT and LAMMPS, respectively. The differences between the ILP and reference sliding data are presented in the third row of Figure S4. The largest deviation of ~1.5 meV/atom occurs for the heterogeneous graphene/*h*-BN junction. This deviation can be further reduced by using the parameters of Table S2 leading to a maximal deviation of ~0.6 meV/atom for the graphene/*h*-BN heterojunction as shown in Figure S5.

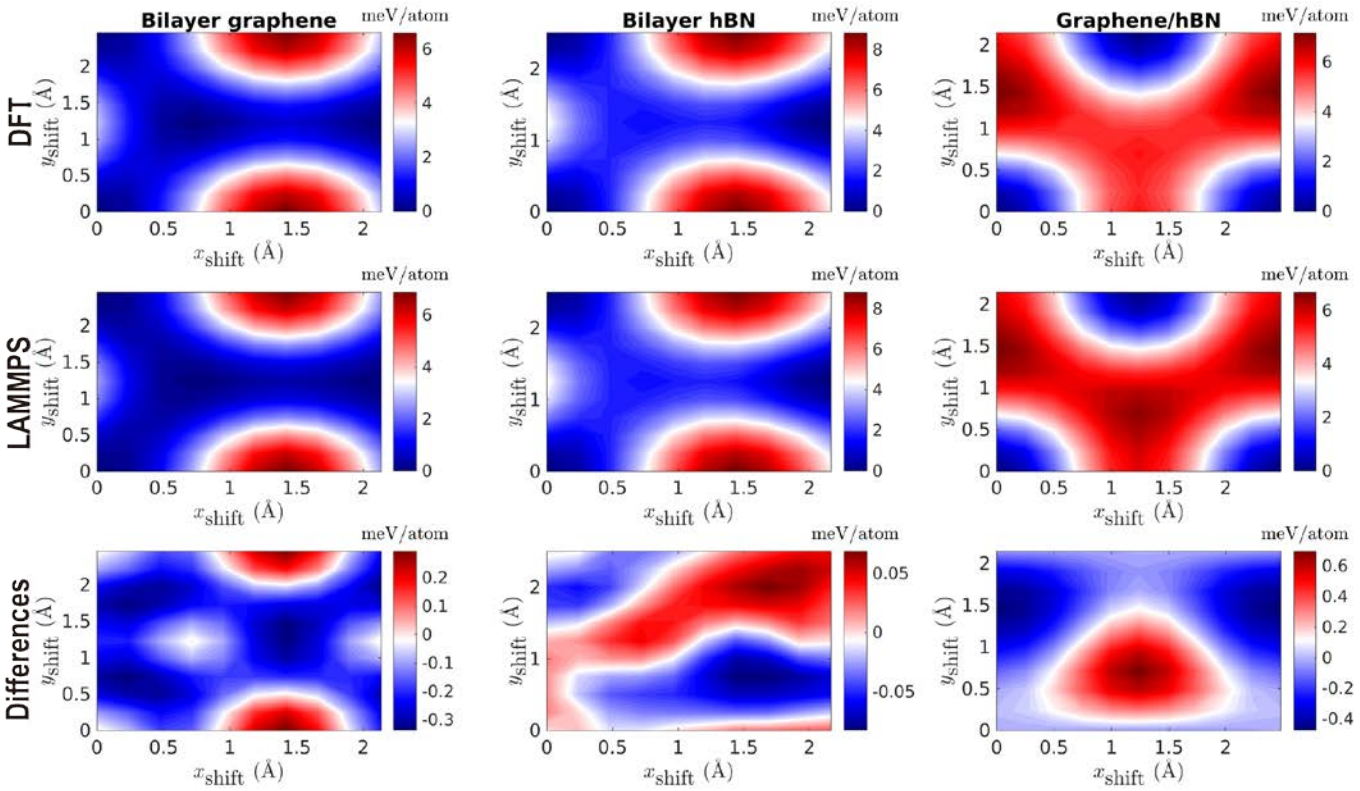

Figure S5*: Sliding energy surfaces of the various periodic structures considered. The first and second rows present the sliding energy surface of graphene/graphene, h-BN/h-BN and graphene/h-BN bilayers calculated using dispersion augmented DFT and the LAMMPS implementation of the refined ILP, respectively. The third row presents their differences. The parameters of Table S2 are used in the ILP calculations.*

2.3 **Binding Energy Curves and Sliding Energy Surfaces Obtained Using the KC Potential**

Figure S6 illustrates the refined parameters (Table S3) of original KC potential (without taper function) benchmark tests for homogenous graphene bilayer. The refined parameters proposed herein provide a satisfactory agreement with the reference binding energy curve within the long-range, near-equilibrium, and sub-equilibrium interlayer separation regimes. This improves upon the original parameterizations for KC potential,[4] which shows larger deviations near equilibrium. Figure S6 e-f presents the differences of the sliding energy surfaces of bilayer graphene, between the original and refined KC potential parameterizations and the DFT reference data, respectively. The corresponding largest absolute deviations are ~0.6 and ~0.06 meV/atom. The refined parameters (Table S4) of modified KC potential (with taper function) give very similar behavior. To avoid unnecessary repetition, we do not show the corresponding plots here.

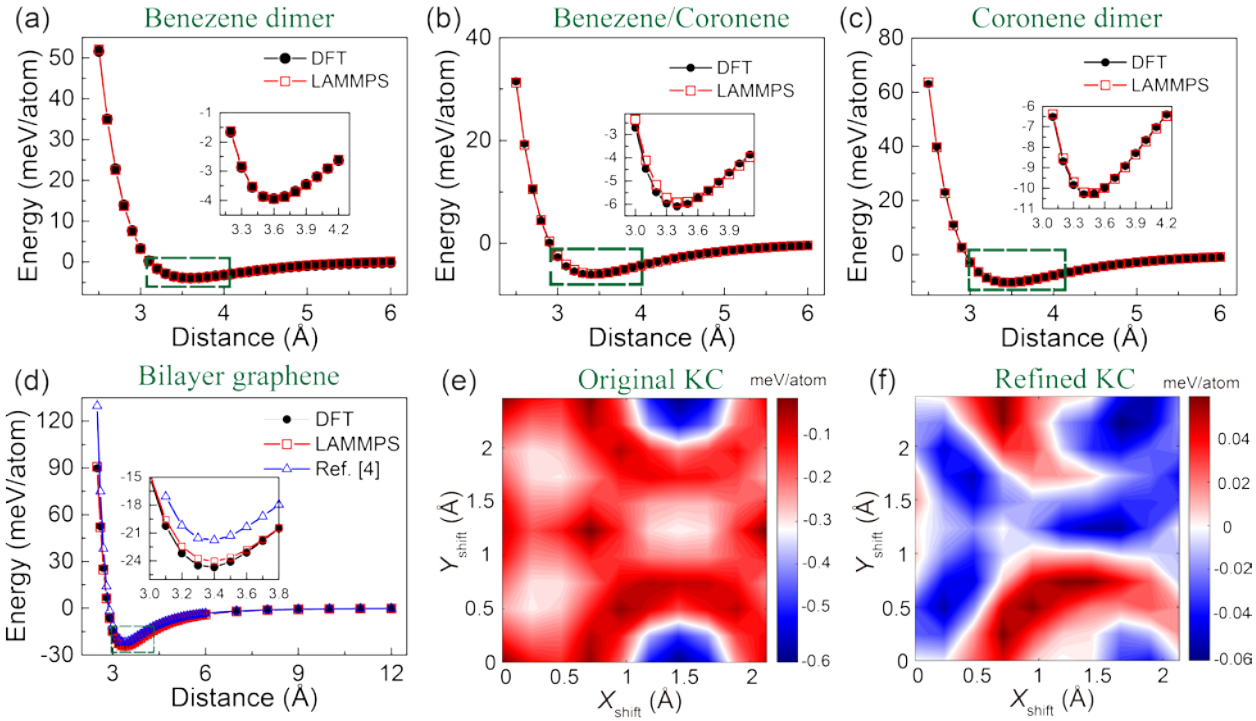

***Figure S6**: Benchmark tests for the KC potential. Binding energy curves calculated for the finite homogenous dimers of (a) Benzene, (b) Benzene/Coronene, (c) Coronene and for (d) periodic bilayer graphene. Energies are reported relative to the infinitely separated interface value and are normalized by the total number of atoms per unit-cell. The insets provide a zoom-in on the equilibrium interlayer separation region. (e) bilayer graphene sliding energy surface difference between the LAMMPS implementation of the original KC potential and dispersion augmented DFT, (f) same as (e) but for refined KC potential. The parameters appearing in Table S3 are used herein.*

3. ILP Parameters Sensitivity Test

In order to check the sensitivity of the friction force results reported in the main text to the choice of ILP parameter set, we compare in Figure S7 the length dependence of static and kinetic friction forces of the GNR/*h*-BN heterojunctions for the two sets of parameters presented in Table S1 (full red circles) and Table S2 (open blue squares). The two sets produce very similar results, indicating that under the simulations conditions used herein the friction forces are relatively insensitive to the corresponding differences between the interaction potentials.

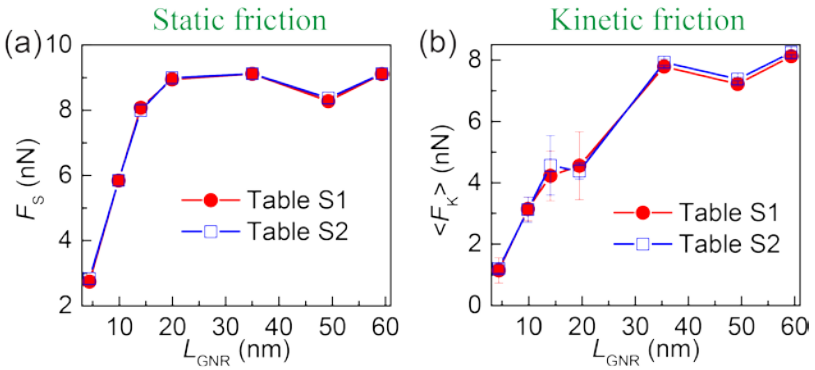

Figure S7*: Sensitivity of the friction forces of a GNR/h-BN heterojunction towards the choice of ILP parameter set. Shown is the length dependence of the (a) static and (b) kinetic friction forces of the GNR calculated using the parameters presented in Table S1 (full red circles) and in Table S2 (open blue squares). The static friction force was evaluated from the maxima of the friction force traces. The kinetic friction force was calculated as* $\langle F_K \rangle = \langle K_{\mathrm{dr}}(V_{\mathrm{dr}}t - X_{\mathrm{edge}}) \rangle$*, where* $\langle \cdot \rangle$ *denotes a steady-state time average. The statistical errors have been estimated using ten different trajectories, each averaged over a time interval of* 1 *ns.*

4. Intra-layer Potential Sensitivity Test

In order to check the sensitivity of the friction force results reported in the main text to the choice of intra-layer potential we compare in Figure S8 the length dependence of static and kinetic friction forces of the GNR/*h*-BN heterojunctions obtained using the AIREBO[14] and the REBO[15] force-fields for graphene. Since the equilibrium intralayer C-C distances obtained with the AIREBO and REBO potential differ (1.3978 and 1.42 Å, respectively), we adjust the lattice constant of the rigid *h*-BN substrate accordingly to get the same lattice mismatch of 1.8 %. The two intra-layer terms produce very similar results indicating that under the simulation conditions used herein the friction forces are relatively insensitive to the choice of intra-layer potential. We note that in all simulations presented in the main text, the AIREBO potential has been used.

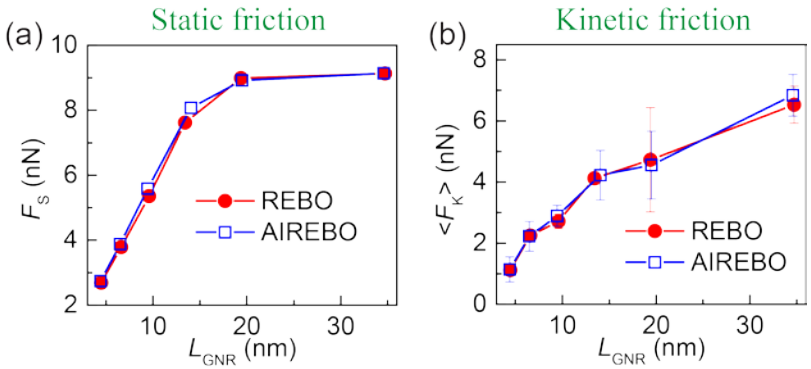

Figure S8*: Sensitivity of the friction forces of a GNR/h-BN heterojunction towards the choice of intra-layer potential. Shown is the length dependence of the (a) static and (b) kinetic friction forces calculated using the REBO (full red circles) and AIREBO (open blue squares) potentials. The statistical errors have been estimated as in Figure S7.*

5. Damping Coefficient Sensitivity Test

In order to check the sensitivity of the friction force results that reported in the main text to the choice of damping coefficients (see Eq. 1 of the main text), we compare in Figure S9 the length dependence of static and kinetic friction forces of the GNR/graphene homogenous junctions obtained using three different values of η^0 spanning two orders of magnitude around the value adopted in the main text, $\eta^0 = 0.1, 1.0, 10.0$ ps^{-1}. While in general we obtained similar qualitative trends, a somewhat increased friction is observed for the highest value considered. This is due to the increasing contribution of the viscous-like friction term of Eq. 1 of the main text. Noting that in typical experiments the pulling velocities are several orders of magnitude lower than those that can be practically simulated, the contribution of viscous-like friction in the simulation is irrelevant for the interpretation of experimental data.

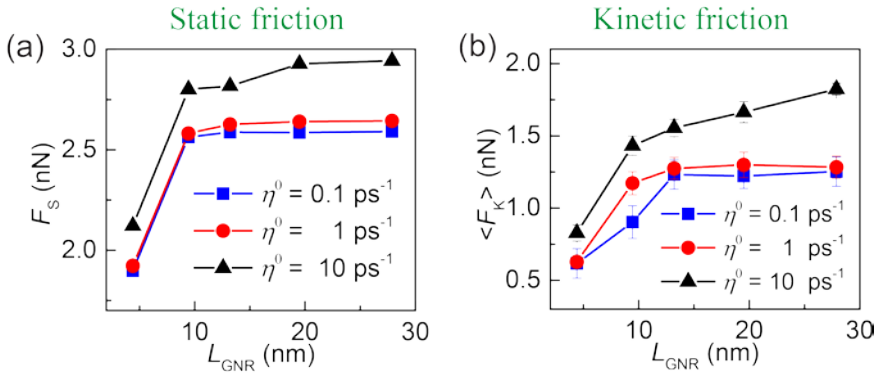

Figure S9*: Sensitivity of the friction forces of a GNR/graphene homogenous junction towards the choice of damping coefficients. Shown is the length dependence of the (a) static and (b) kinetic friction forces calculated using three values of the damping coefficients:* $\eta^0 = 0.1\ ps^{-1}$ *(full blue squares)* $\eta^0 = 1.0\ ps^{-1}$ *(full red circles), and* $\eta^0 = 10.0\ ps^{-1}$ *(full black triangles). The statistical errors have been estimated as in Figure S7.*

6. Propagation Time-Step Sensitivity Test

In order to check the sensitivity of the friction force results reported in the main text to the choice of propagation time-step we compare in Figure S10 the friction force traces of a 4.5 nm GNR sliding atop a graphene substrate obtained using a time-step of 1 fs (as in the main text) and 0.25 fs. We find that, despite the presence of light hydrogen atoms, a time-step of 1 fs is sufficient to provide converged results.[16]

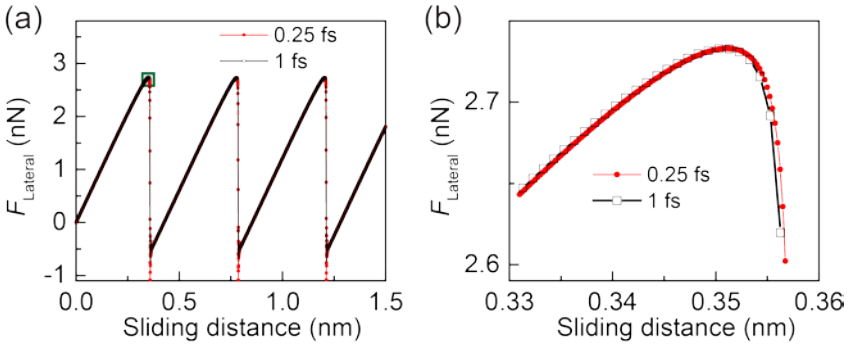

Figure S10*: Sensitivity of the friction force traces of a 4.5 nm GNR sliding atop a graphene substrate towards the choice of propagation time-step. Shown is (a) the full steady-state friction force trace and (b) a zoom-in on the peak region obtained using a time step of 1 fs (open black squares) and 0.25 fs (full red circles).*

7. Simulation Protocol at Finite Temperature

The simulations at room temperature (300 K) were performed using a Langevin thermostat applied to all slider atoms. The equation of motion is as follows:

$$m_i\ddot{\boldsymbol{r}}_i = -\boldsymbol{\nabla}_i\left(V^{\text{inter}} + V^{\text{intra}}\right) - \sum_{\alpha=x,y,z}\eta_\alpha(z_i)m_i\dot{\boldsymbol{r}}_{i,\alpha} + K_\parallel(\boldsymbol{r}_i - \boldsymbol{r}^{\text{stage}})\delta_{i,i_{\text{edge}}} + \xi_\alpha^i(t), \quad \text{(S9)}$$

where m_i is the mass of atom i, $\boldsymbol{r}_i$ is its position, and V^{inter} and V^{intra} are the interlayer and intra-layer interaction potentials, respectively. The second term in Eq. S9 represents viscous damping applied in all directions $\alpha = x, y, z$ to all GNR atoms, the third term is the driving spring force, which is applied only to the three rightmost edge atoms in the lateral directions, and the last term is a random force acting on the i^{th} particle in all directions ($\alpha = x, y, z$), satisfying the fluctuation-dissipation theorem：

$$\langle\xi_\alpha^i(t)\xi_\beta^j(t')\rangle = 2\eta_\alpha m_i k_B T\delta(t-t')\delta_{\alpha\beta}\delta_{ij},\ i,j = 1,2,\cdots N;\alpha,\beta = x,y,z \quad \text{(S10)}$$

The following protocol was adopted in the simulations at finite temperature. First, the system was equilibrated at 300 K for 400 ps with a time step of 0.5 fs, in absence of the pulling apparatus. After equilibration, the friction simulations were carried out adopting the same pulling velocity and springs' constant used in the zero temperature simulations (see main text).

8. Theoretical Estimation of the Characteristic Stress Decay Length

As mentioned in the main text, for commensurate contacting surfaces such as the aligned GNR/graphene interface the shear-induced stress distribution across the GNR can be described by a simplified one-dimensional model.[17] The characteristic stress decay length predicted by this model is given by $L_c = L_{\text{GNR}}\sqrt{K_{\text{GNR}}/K_{\text{Interface}}}$, where L_{GNR} is the length of the GNR, $K_{\text{Interface}}$ is the interfacial shear stiffness between the GNR and the substrate and $K_{\text{GNR}} = Ehb/L_{\text{GNR}}$ is the in-plane stiffness of the GNR. Here, *E*, *h*, and *b* are the Young's modulus, the thickness, and width of the GNR, respectively.

The interfacial shear stiffness, $K_{\text{Interface}}$, has been evaluated by shifting the fully relaxed GNR rigidly over the graphene surface along the aligned sliding direction and fitting the deepest well obtained along the sliding potential energy curve to a parabola. As expected for commensurate contacts, this stiffness grows linearly with the GNR length (see Figure S11a). To evaluate the GNR's in-plane stiffness we adopted the

values $Eh = 26.6$ eV/Å^2 and b = 0.726 nm.[18] A fit of the data reported in Figure S11a (see red line) yielded $K_{\mathrm{Interface}}/L_{\mathrm{GNR}} = 87.66 \pm 0.21$ eV/nm^3, giving $L_c \approx 4.6948 \pm 0.0056$ nm, somewhat larger than that obtained from fitting the MD simulation results (4.14 nm). The main reason for this discrepancy is that the theoretical estimation is based on a one-dimensional model, while the MD simulations allow for atomic motions in all directions. To prove this point, we performed additional simulation while freezing the atomic degrees of freedom perpendicular to the pulling direction. The resulting GNR stress-distribution color maps of the stress profile before the first slip event are illustrated in Figure S11b and c. By fitting the stress profile with an exponential function, we obtained a characteristic stress decay length of 4.66 nm, in better agreement with the value predicted by the one-dimensional theory.

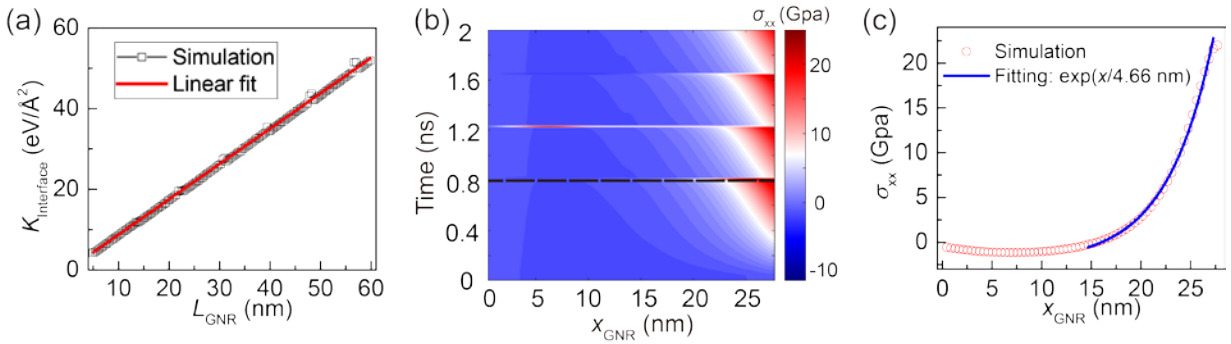

Figure S11*: Estimation of the characteristic stress decay length. (a) The interfacial shear stiffness for the aligned homogeneous GNR/graphene junction as a function of the GNR length. The open black squares are simulation results and the red line is a linear fit. The sudden jumps in the simulation results are due to edge effects corresponding to a change in the local stacking of the leading edge atoms of the relaxed GNR relative to the graphene substrate. (b) Color maps showing the stress distribution along the GNR as a function of time for the aligned GNR/graphene junction. Here, all atoms within the GNR are constrained to move only along the pulling direction. (c) Open red circles show a cross section of the color map appearing in panel (b) at the onset of global sliding (dashed black line in panel (b)). The blue curve in panel (c) is an exponential fit with a characteristic stress decay length of 4.66 nm.*

9. Stacking Mode of the Leading GNR Edge Atoms for Heterogeneous GNR/*h*-BN Junctions

To explain the sharp jumps between two distinct values of static friction observed in GNR/*h*-BN heterojunctions with increasing ribbon length (Figure 2b in the main text), we show in Figure S12 the stacking mode of the leading edge of the ribbon for L_{GNR}=37.76 nm and L_{GNR}=48.08 nm, respectively, at the onset of a sliding event. We find that when the GNR exhibits even (odd) number of buckles, its leading

edge atoms (marked in red) are positioned in an energetically (un)favorable stacking mode.

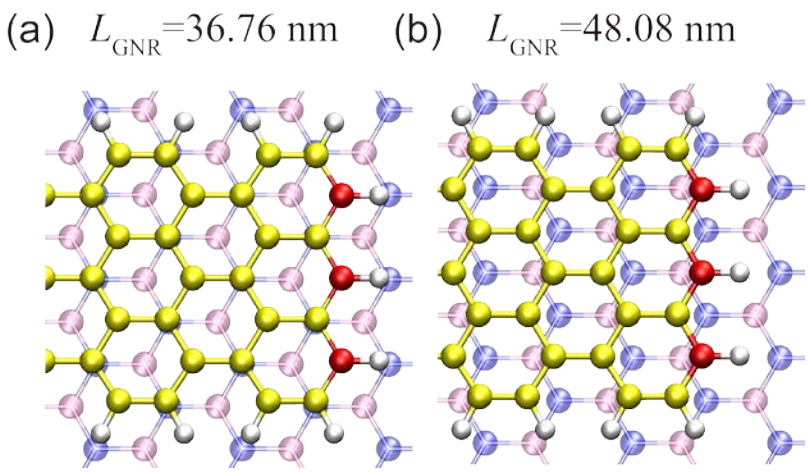

Figure S12*: Stacking modes of the GNR leading edge atoms atop an h-BN substrate obtained for a ribbon length of (a) 37.76 nm and (b) 48.08 nm at the onset of a sliding event. Mauve, blue, yellow, and grey spheres represent boron, nitrogen, carbon, and hydrogen atoms, respectively. The leading edge atoms of the GNR are marked in red.*

10. Evolution of Potential Energy During Sliding at 45 degrees

To explain the origin of the rotation of GNRs from a pulling direction of 45 degrees (with respect to the armchair axis) to 60 degrees, we calculated the potential energy as a function of sliding distance during the motion of 4.5 and 27.5 nm long GNRs on graphene and *h*-BN (see Figure S13). Panels a-d of Figure S13 clearly demonstrate that upon rotation from the pulling direction of 45 degrees to a 60 degrees orientation the potential energy experienced by the GNR drops. To further elucidate this point, we carried out additional geometry optimizations for the 27.5 nm long GNR deposited on graphene or *h*-BN at different misaligned rotation angles relative to the substrate. Panels e-f of Figure S13 show that both homogenous and heterogeneous junctions, have lower energy at the aligned interfaces, corresponding to multiples of 60 degrees. We note that a similar effect has been previously demonstrated to be at the origin of the angular reorientation of graphene nano-flakes sliding over graphite.[19, 20]

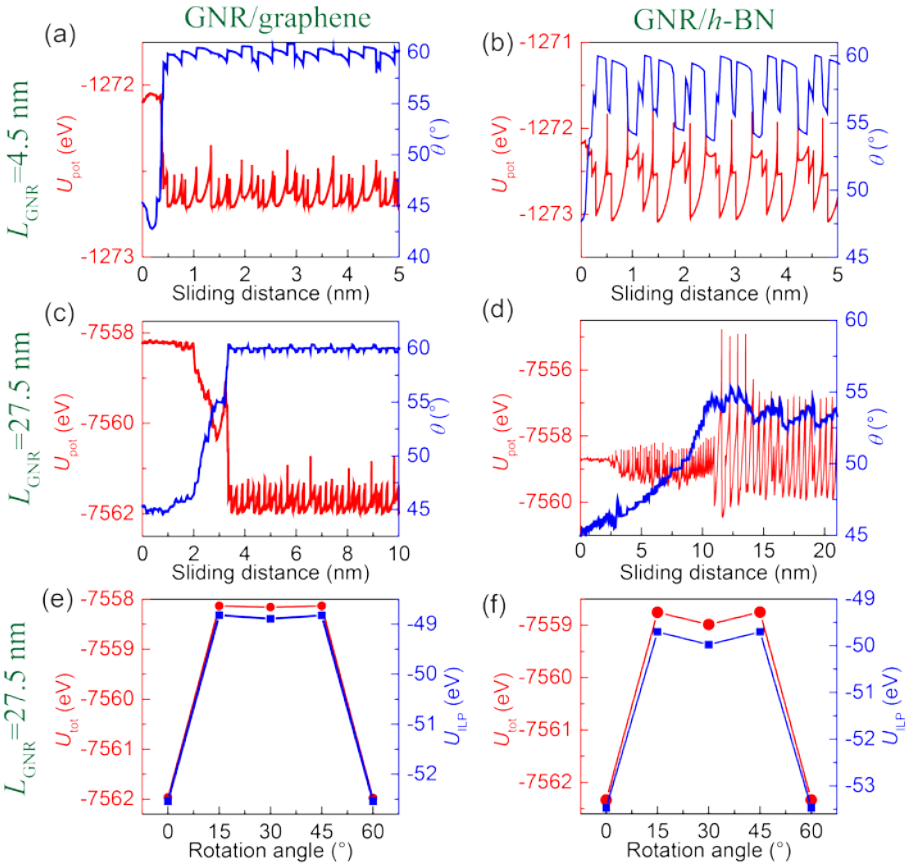

Figure S13. *Frictional motion of GNRs pulled along a direction of* 45° *with respect to the armchair direction of graphene ((a) and (c)) and h-BN ((b) and (d)) substrates. Both the total potential energy (left axis, red) and the average angle (right axis, blue) are presented as a function of sliding distance for* $L_{GNR} = 4.5\ nm$ *(panels (a) and (b)) and* $27.5\ nm$ *(panels (c) and (d)). The total potential energy (left axis) and interfacial energy (right axis) of the longer GNR on graphene and h-BN with different rotation angles are presented in panels (e) and (f), respectively.*

REFERENCES

(1) Maaravi, T.; Leven, I.; Azuri, I.; Kronik, L.; Hod, O. *J. Phys. Chem. C* **2017,** 121, 22826-22835.
(2) Leven, I.; Maaravi, T.; Azuri, I.; Kronik, L.; Hod, O. *J. Chem.Theory Comput.* **2016,** 12, 2896-905.
(3) Leven, I.; Azuri, I.; Kronik, L.; Hod, O. *J. Chem. Phys.* **2014,** 140, 104106.
(4) Kolmogorov, A. N.; Crespi, V. H. *Phys. Rev. B* **2005,** 71, 235415.
(5) Tkatchenko, A.; Scheffler, M. *Phys. Rev. Lett.* **2009,** 102, 073005.
(6) Heyd, J.; Scuseria, G. E.; Ernzerhof, M. *J. Chem. Phys.* **2003,** 118, 8207-8215.
(7) Heyd, J.; Scuseria, G. E. *J. Chem. Phys.* **2004,** 120, 7274-7280.
(8) Heyd, J.; Scuseria, G. E. *J. Chem. Phys.* **2004,** 121, 1187-1192.
(9) Tkatchenko, A.; DiStasio, R. A.; Car, R.; Scheffler, M. *Phys. Rev. Lett.* **2012,** 108, 236402.
(10) Ambrosetti, A.; Reilly, A. M.; Jr., R. A. D.; Tkatchenko, A. *J. Chem. Phys.* **2014,** 140, 18A508.
(11) Byrd, R. H.; Gilbert, J. C.; Nocedal, J. *Math. Program.* **2000,** 89, 149-185.
(12) Waltz, R. A.; Morales, J. L.; Nocedal, J.; Orban, D. *Math. Program.* **2006,** 107, 391-408.
(13) Plimpton, S. *J. Comput. Phys.* **1995,** 117, 1-19.
(14) Stuart, S. J.; Tutein, A. B.; Harrison, J. A. *J. Chem. Phys.* **2000,** 112, 6472-6486.
(15) Brenner, D. W.; Shenderova, O. A.; Harrison, J. A.; Stuart, S. J.; Ni, B.; Sinnott, S. B. *J. Phys.: Condens. Matter* **2002,** 14, 783-802.
(16) Jo, J. C.; Kim, B. C. *B. Kor. Chem. Soc.* **2000,** 21, 419-424.
(17) Capozza, R.; Urbakh, M. *Phys. Rev. B* **2012,** 86, 085430.
(18) Zhang, D. B.; Akatyeva, E.; Dumitrică, T. *Phys. Rev. Lett.* **2011,** 106, 255503.
(19) Filippov, A. E.; Dienwiebel, M.; Frenken, J. W. M.; Klafter, J.; Urbakh, M. *Phys. Rev. Lett.* **2008,** 100, 046102.
(20) Feng, X.; Kwon, S.; Park, J. Y.; Salmeron, M. *ACS nano* **2013,** 7, 1718-1724.